MgB_2Se_4 Spinels (B = Sc, Y, Er, Tm) as Potential Mg-Ion Solid Electrolytes – Partial Ionic Conductivity and the Ion Migration Barrier

*Clarissa Glaser, Manuel Dillenz, Kanchan Sarkar, Mohsen Sotoudeh, Zhixuan Wei, Sylvio Indris, Ruben Maile, Marcus Rohnke, Klaus Müller-Buschbaum, Axel Groß and Jürgen Janek**

Supporting Information

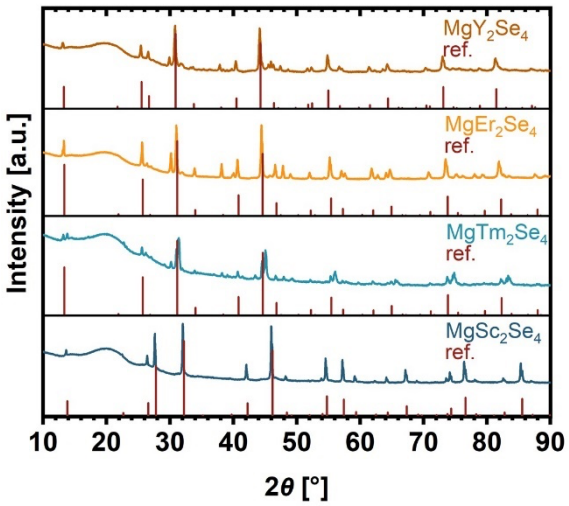

Figure S1. XRD patterns of spinels $MgSc_2Se_4$, $MgTm_2Se_4$, $MgEr_2Se_4$ and MgY_2Se_4 synthesized via one-step route. Data for $MgSc_2Se_4$ reproduced under terms of the CC BY-NC-ND 4.0 license.[1] Copyright © 2023, C. Glaser et al., *Adv. Energy. Matter*. 2023, published by Wiley-VCH GmbH.

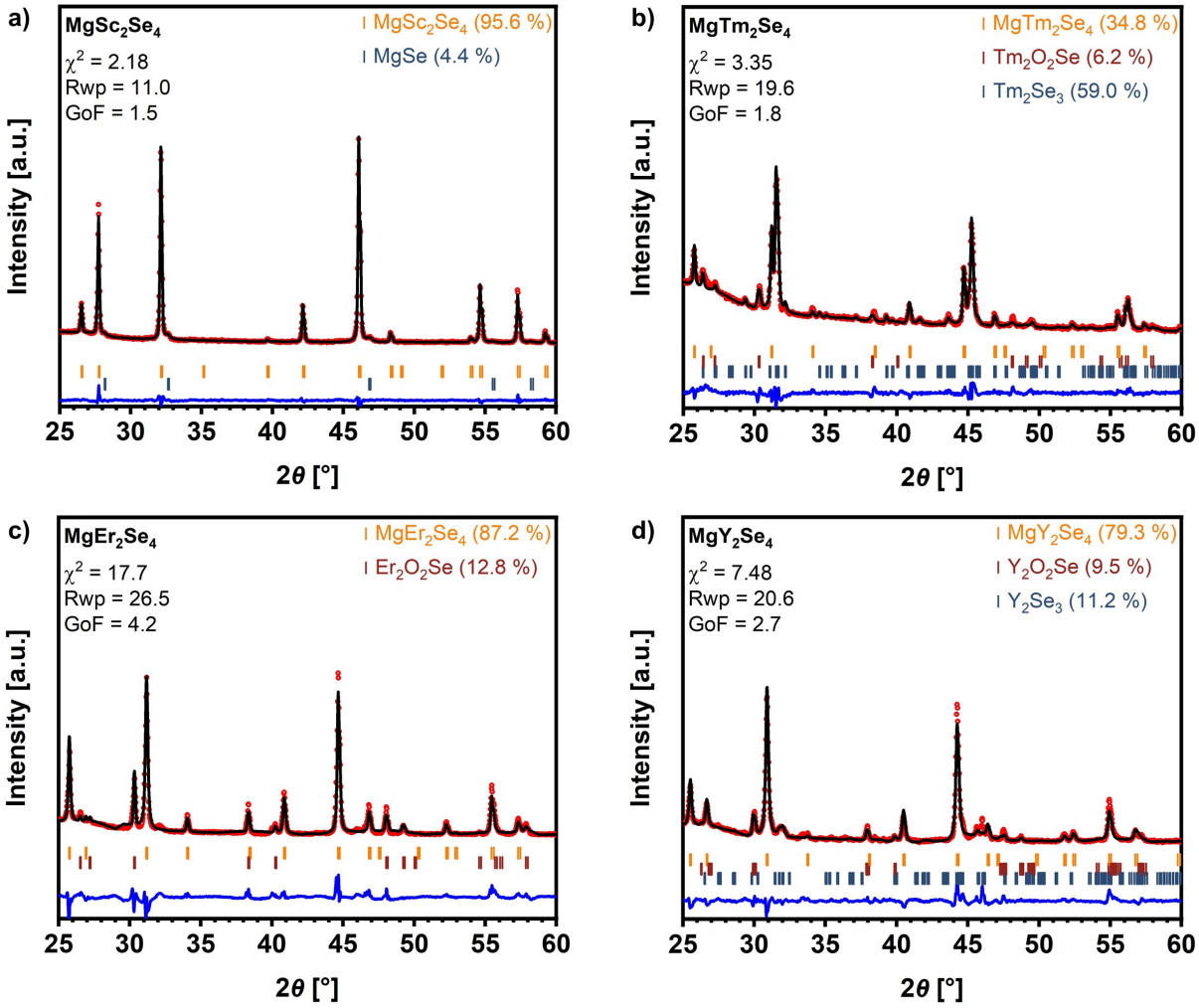

Figure S2. Rietveld refinement of one-step synthesized a) $MgSc_2Se_4$, b) $MgTm_2Se_4$, c) $MgEr_2Se_4$ and d) MgY_2Se_4, based on the XRD pattern from **Figure S1**. The observed and the calculated curves are shown in red and black, and the resulting difference curve is presented in blue. Data for $MgSc_2Se_4$ reproduced under terms of the CC BY-NC-ND 4.0 license.[1] Copyright © 2023, C. Glaser et al., *Adv. Energy. Matter*. 2023, published by Wiley-VCH GmbH.

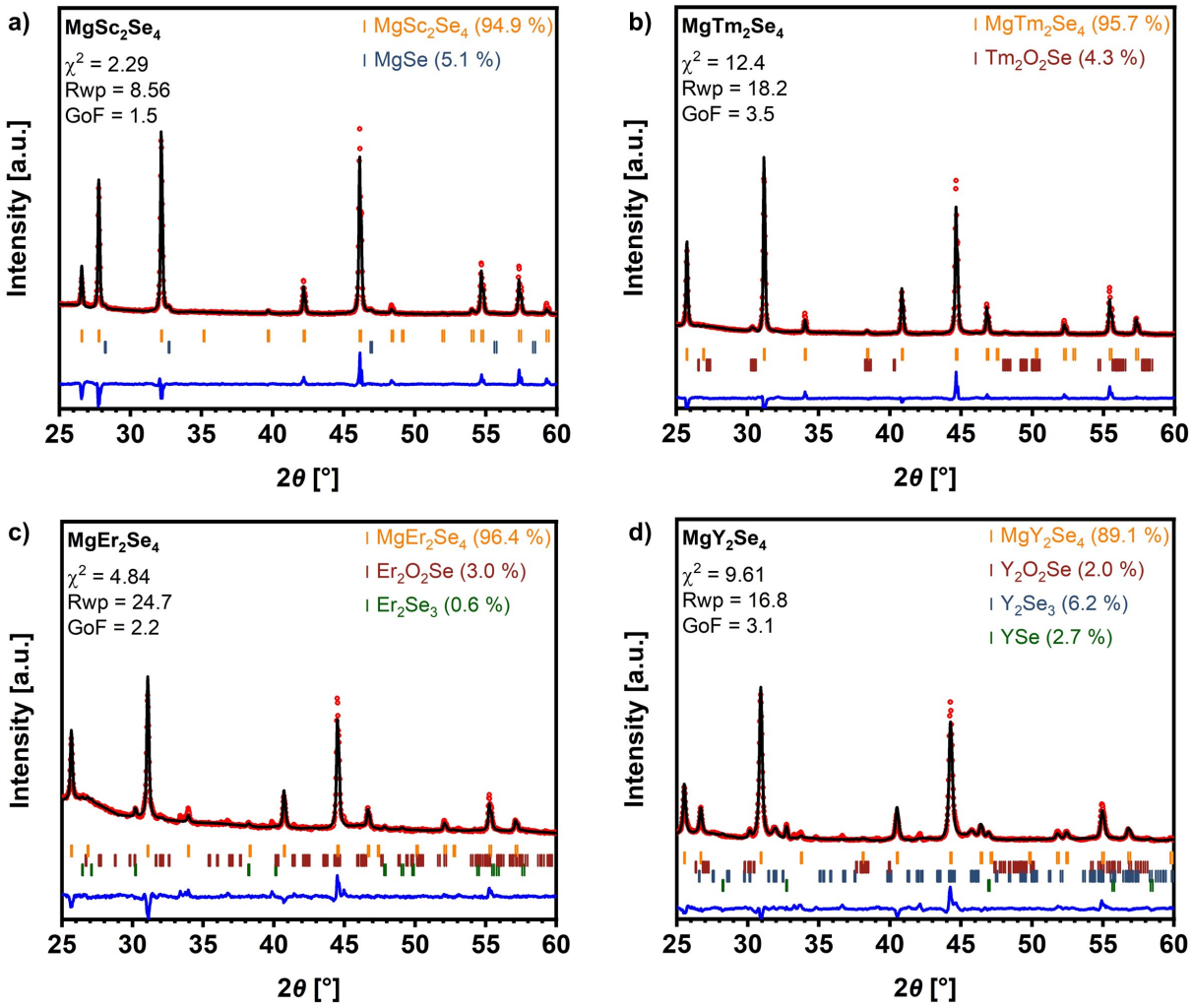

Figure S3. Rietveld refinement of two-step synthesized a) $MgSc_2Se_4$, b) $MgTm_2Se_4$, c) $MgEr_2Se_4$ and d) MgY_2Se_4, based on the XRD pattern for **Figure 1b**. The observed and the calculated curves are shown in red and black, and the resulting difference curve is presented in blue. Data for $MgSc_2Se_4$ reproduced under terms of the CC BY-NC-ND 4.0 license.[1] Copyright © 2023, C. Glaser et al., *Adv. Energy. Matter*. 2023, published by Wiley-VCH GmbH.

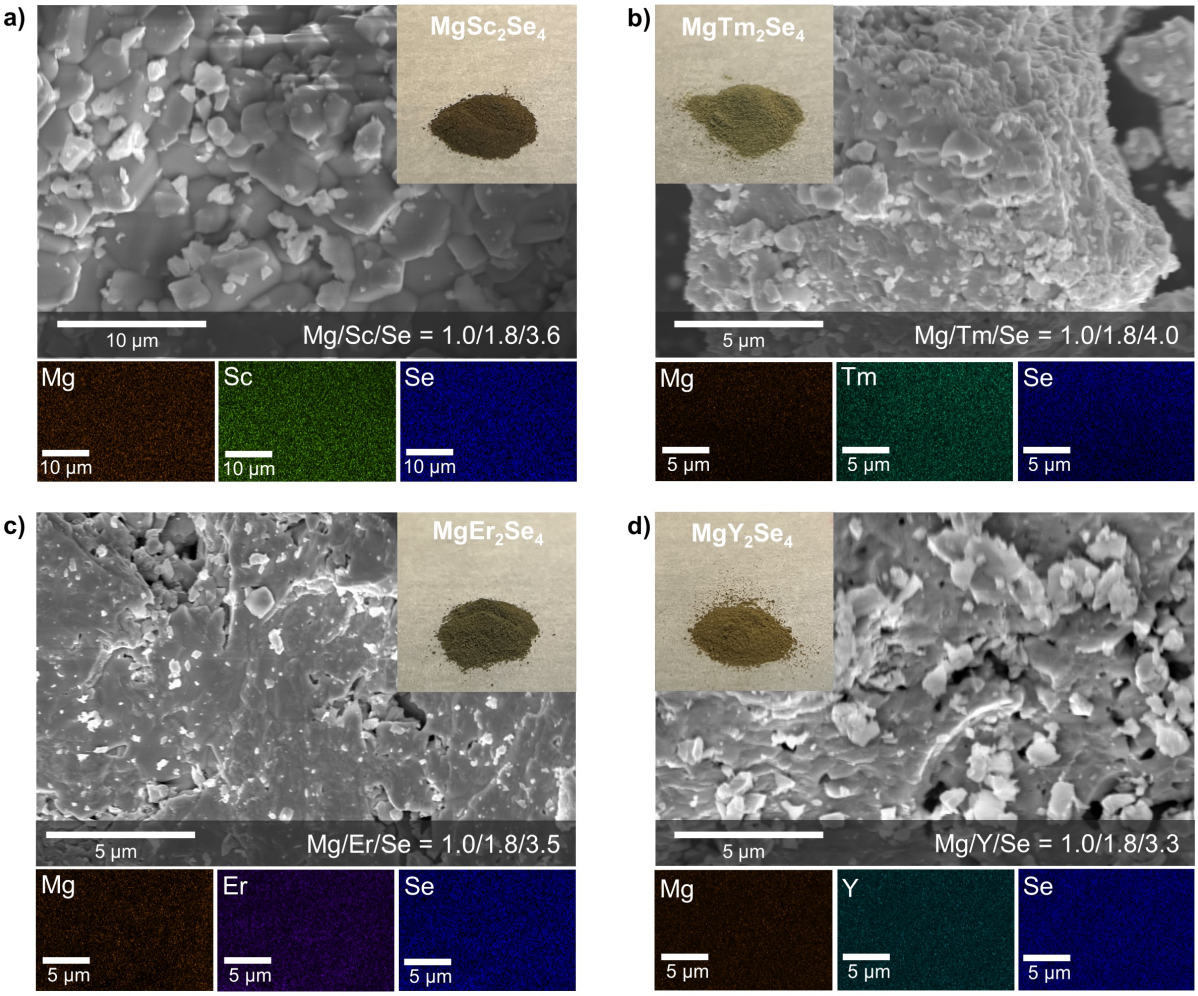

Figure S4. SEM images and light optical images of a) $MgSc_2Se_4$ powder, b) $MgTm_2Se_4$ powder, c) $MgEr_2Se_4$ powder and d) MgY_2Se_4 powder with EDS mapping of the corresponding elements Mg, Sc/Tm/Er/Y and Se.

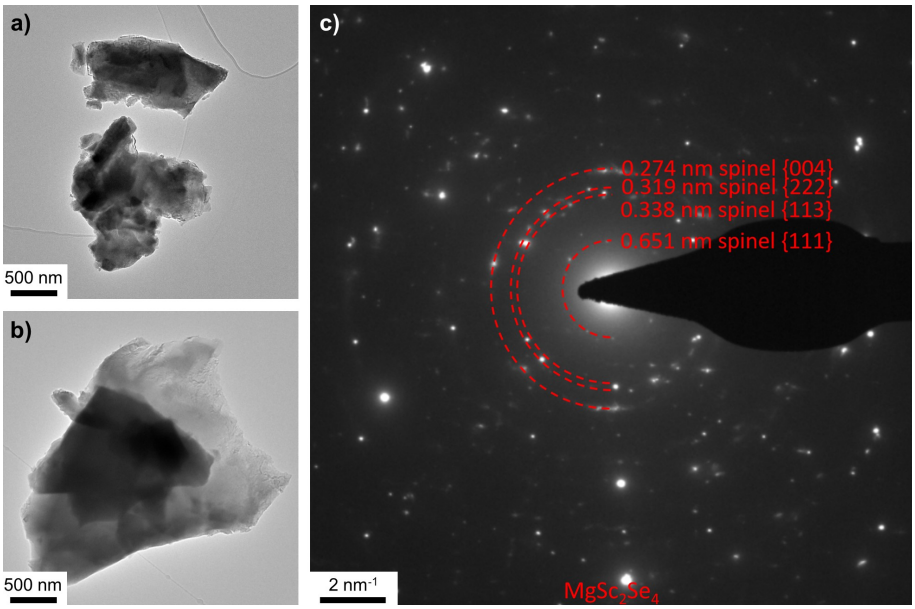

Figure S5. a-b) TEM images of $MgSc_2Se_4$ particles (one-step synthesis) with a size of 1-3 µm and c) SAED pattern confirming the synthesis of the $MgSc_2Se_4$ spinel phase. Reproduced under terms of the CC BY-NC-ND 4.0 license.[1] Copyright © 2023, C. Glaser et al., *Adv. Energy. Matter*. 2023, published by Wiley-VCH GmbH.

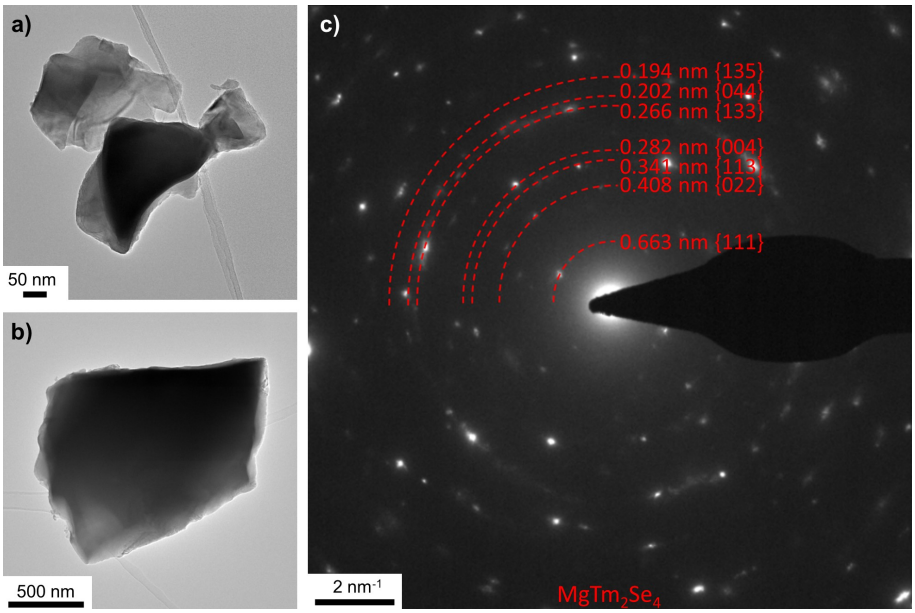

Figure S6. a-b) TEM images of $MgTm_2Se_4$ particles (two-step synthesis) with a size of 0.5-1.5 µm and c) SAED pattern confirming the synthesis of the $MgTm_2Se_4$ spinel phase.

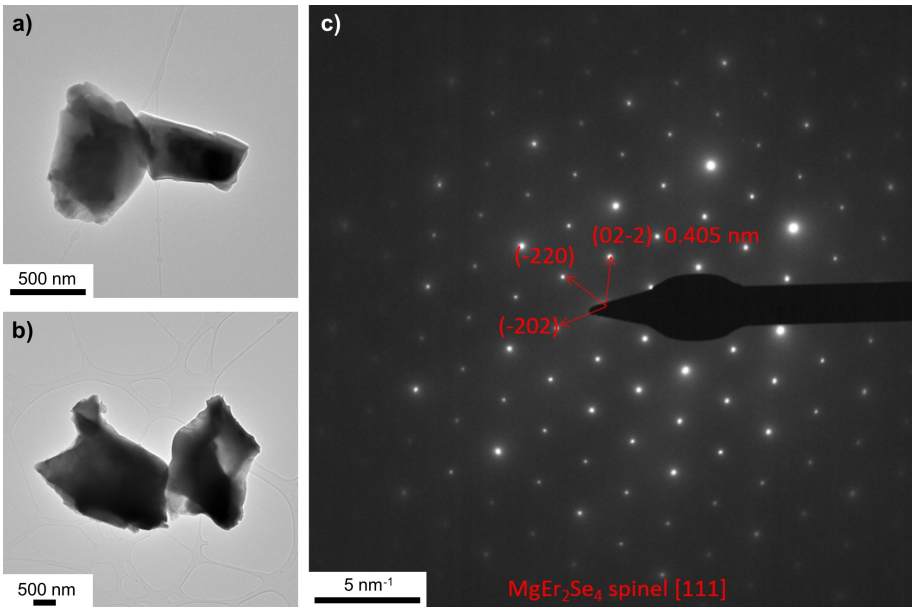

Figure S7. a-b) TEM images of $MgEr_2Se_4$ particles (two-step synthesis) with a size of 0.5-3 µm and c) SAED pattern confirming the synthesis of the $MgEr_2Se_4$ spinel phase.

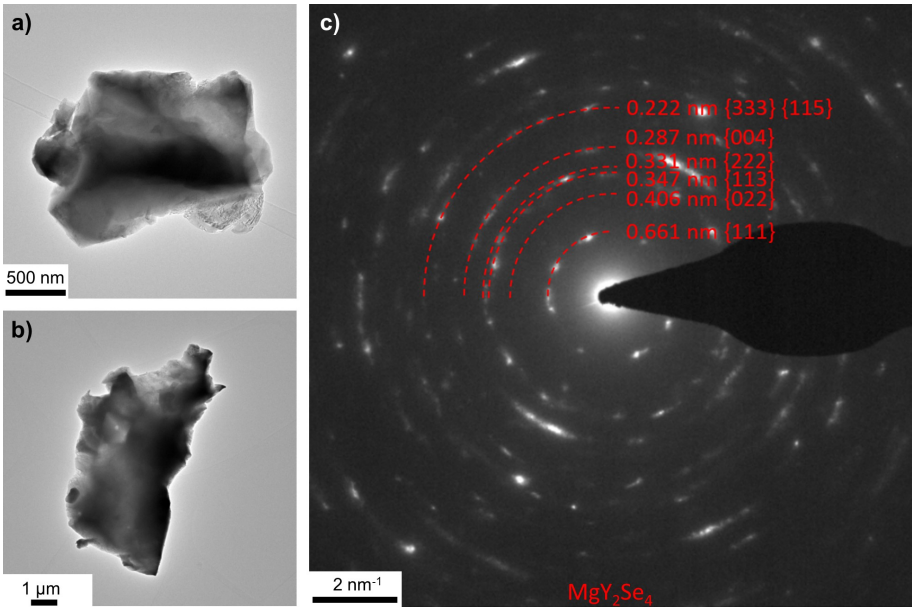

Figure S8. a-b) TEM images of MgY_2Se_4 particles (two-step synthesis) with a size of 1-10 µm and c) SAED pattern confirming the synthesis of the MgY_2Se_4 spinel phase.

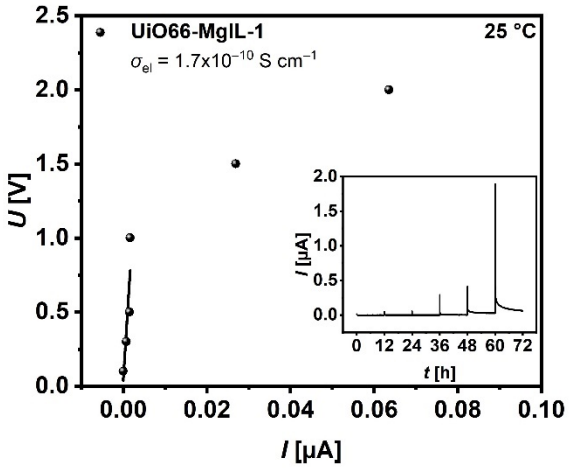

Figure S9. DC polarization data of a SS|UiO66-MgIL|SS cell obtained at different voltages (0.1, 0.3, 0.5, 1.0, 1.5 and 2.0 V, held for 12 h, shown in the inset) with linear fit of the ohmic electronic behavior at 25 °C. Reproduced under terms of the CC BY-NC-ND 4.0 license.[1] Copyright © 2023, C. Glaser et al., *Adv. Energy. Matter*. 2023, published by Wiley-VCH GmbH.

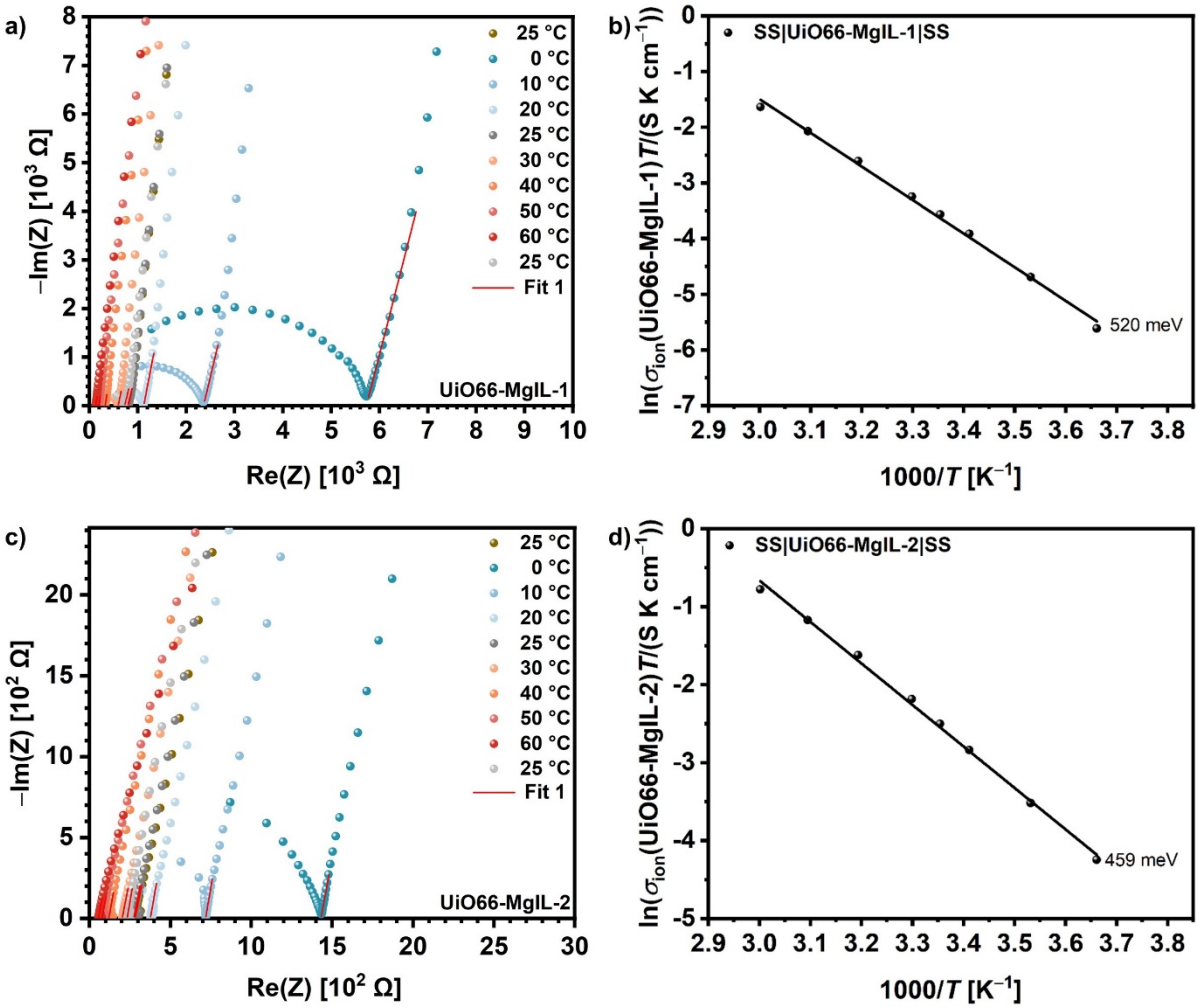

Figure S10. Fitted Nyquist plots of SS|UiO66-MgIL|SS cell at different temperatures ranging from 0 °C to 60 °C of a) batch UiO66-MgIL-1 and b) batch UiO66-MgIL-2 and corresponding Arrhenius plots in b) and d). Data for UiO66-MgIL-1 reproduced under terms of the CC BY-NC-ND 4.0 license.[1] Copyright © 2023, C. Glaser et al., *Adv. Energy. Matter*. 2023, published by Wiley-VCH GmbH.

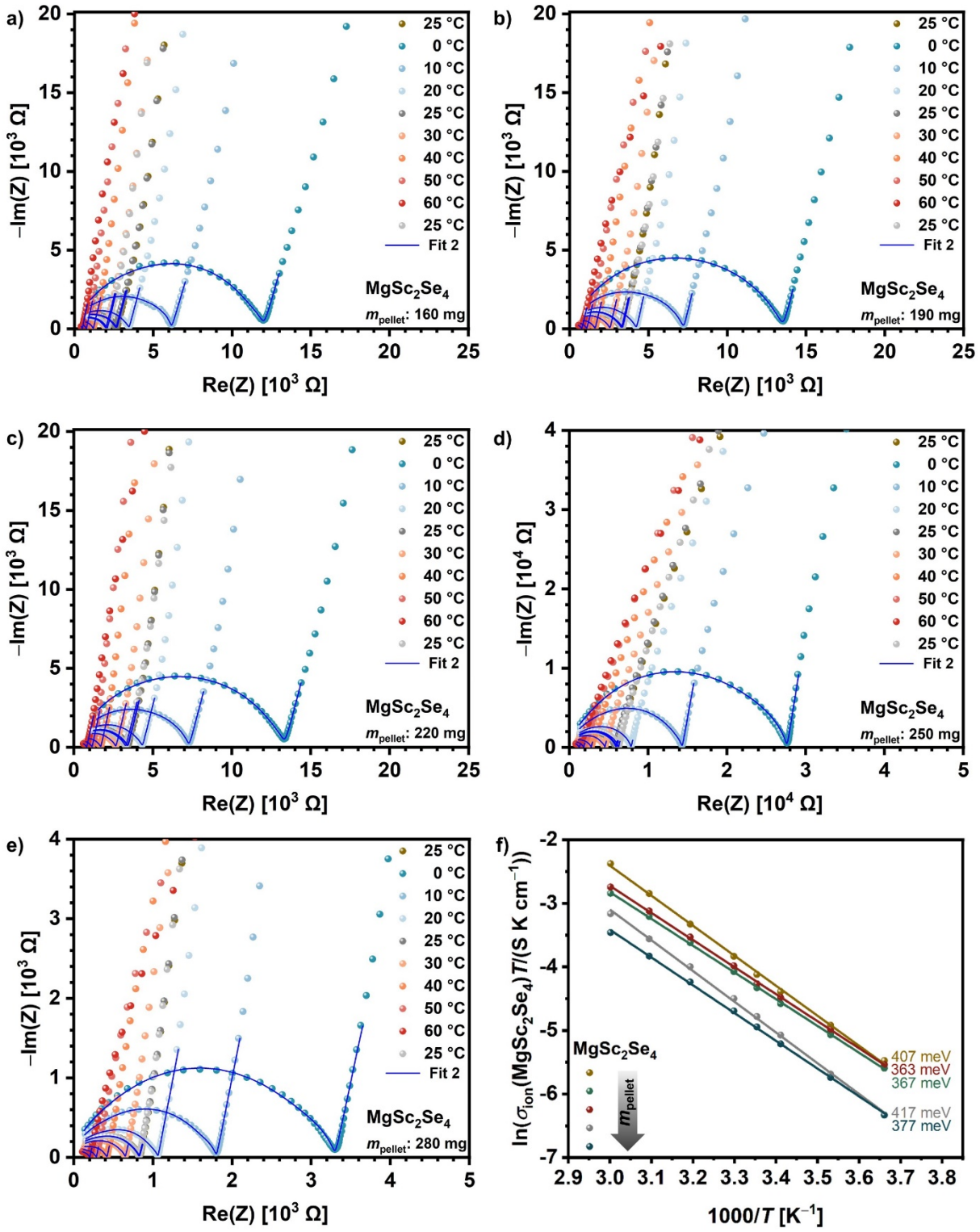

Figure S11. Fitted Nyquist plots of SS|UiO66-MgIL|$MgSc_2Se_4$|UiO66-MgIL|SS cells at different temperatures ranging from 0 °C to 60 °C using a spinel pellet mass/thickness of a) 160 mg/0.80 mm, b) 190 mg/0.88 mm, c) 220 mg/1.10 mm, d) 250 mg/1.14 mm and e) 280 mg/1.40 mm; and f) Arrhenius plots of the ionic conductivity of $MgSc_2Se_4$ for each cell. Reproduced under terms of the CC BY-NC-ND 4.0 license.[1] Copyright © 2023, C. Glaser et al., *Adv. Energy. Matter*. 2023, published by Wiley-VCH GmbH.

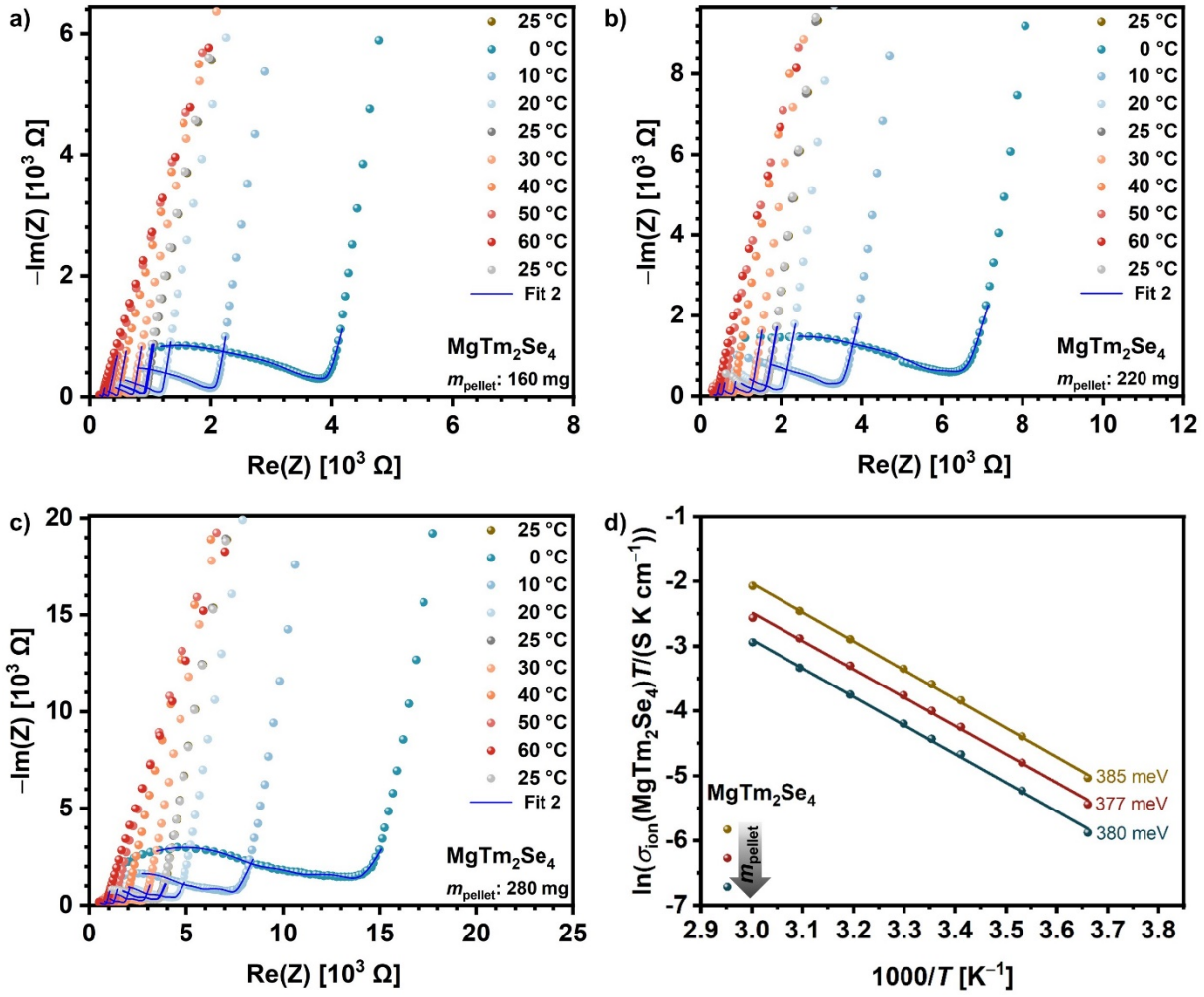

Figure S12. Fitted Nyquist plots of SS|UiO66-MgIL|$MgTm_2Se_4$|UiO66-MgIL|SS cells at different temperatures ranging from 0 °C to 60 °C using a spinel pellet mass/thickness of a) 160 mg/0.46 mm, b) 220 mg/0.62 mm, and c) 280 mg/1.00 mm; and f) Arrhenius plots of the ionic conductivity of $MgTm_2Se_4$ for each cell.

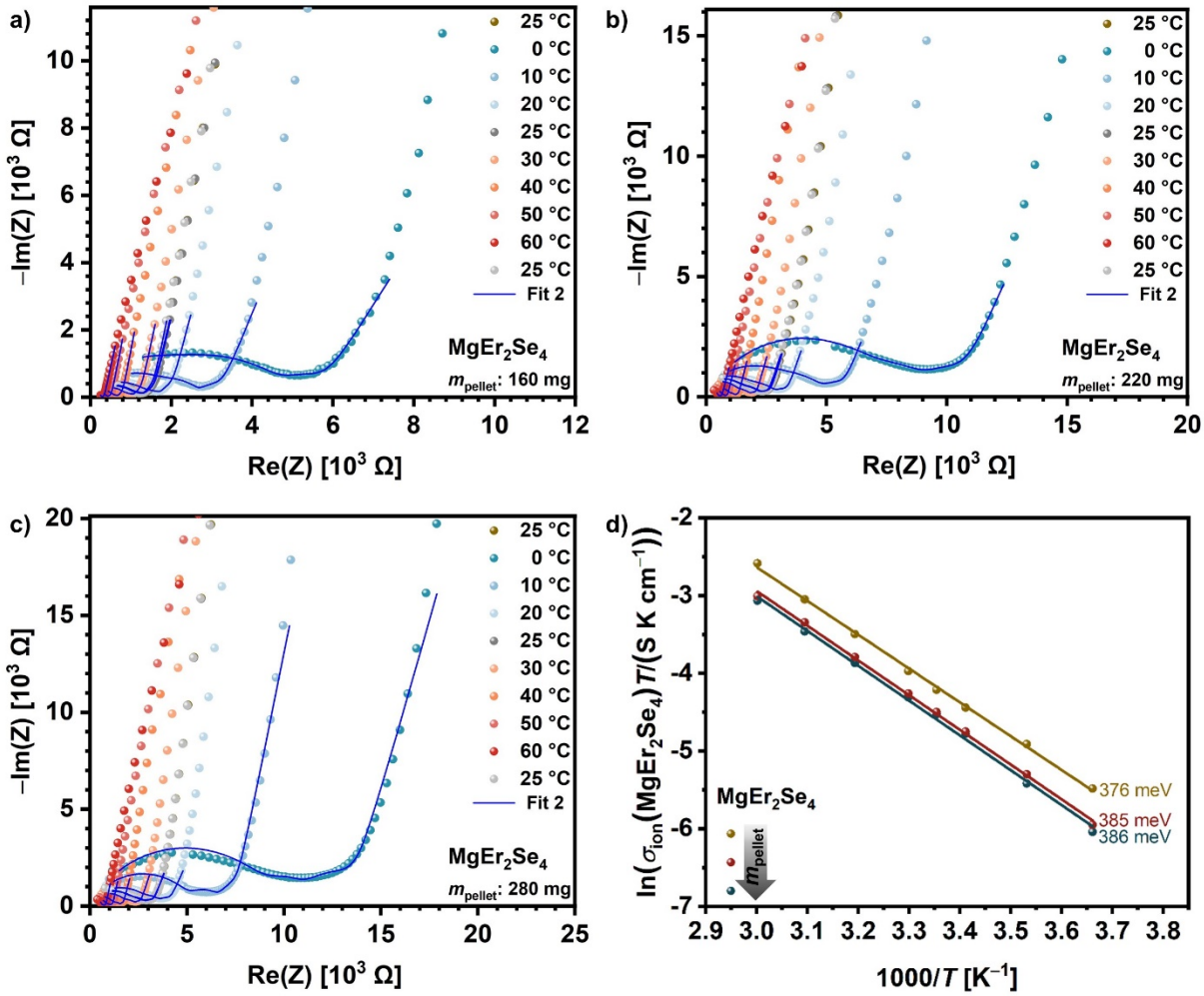

Figure S13. Fitted Nyquist plots of SS|UiO66-MgIL|$MgEr_2Se_4$|UiO66-MgIL|SS cells at different temperatures ranging from 0 °C to 60 °C using a spinel pellet mass/thickness of a) 160 mg/0.50 mm, b) 220 mg/0.68 mm, and c) 280 mg/0.82 mm; and f) Arrhenius plots of the ionic conductivity of $MgEr_2Se_4$ for each cell.

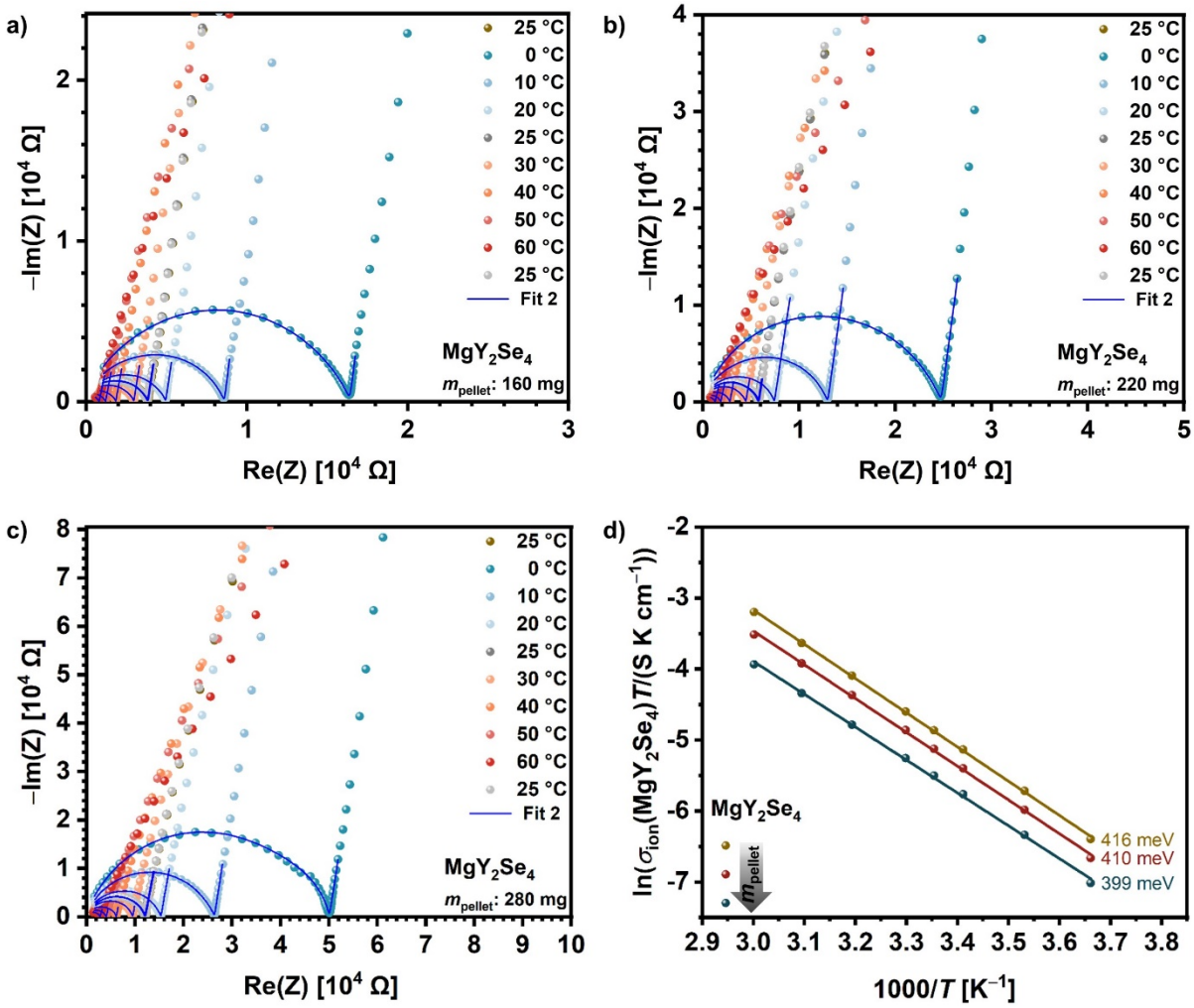

Figure S14. Fitted Nyquist plots of SS|UiO66-MgIL|MgY_2Se_4|UiO66-MgIL|SS cells at different temperatures ranging from 0 °C to 60 °C using a spinel pellet mass/thickness of a) 160 mg/0.72 mm, b) 220 mg/0.86 mm, and c) 280 mg/1.26 mm; and f) Arrhenius plots of the ionic conductivity of MgY_2Se_4 for each cell.

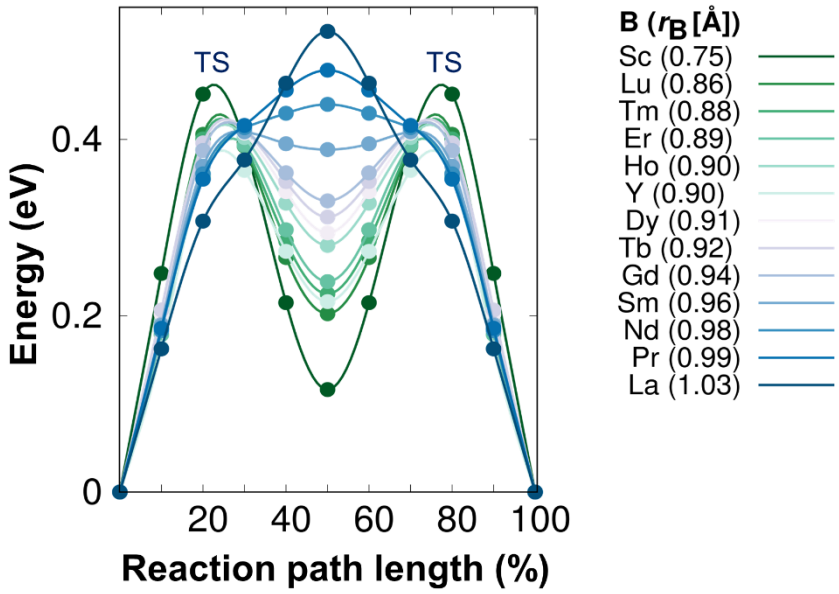

Figure S15. The energy along the migration path for MgB_2S_4 spinel compounds calculated by the NEB method.

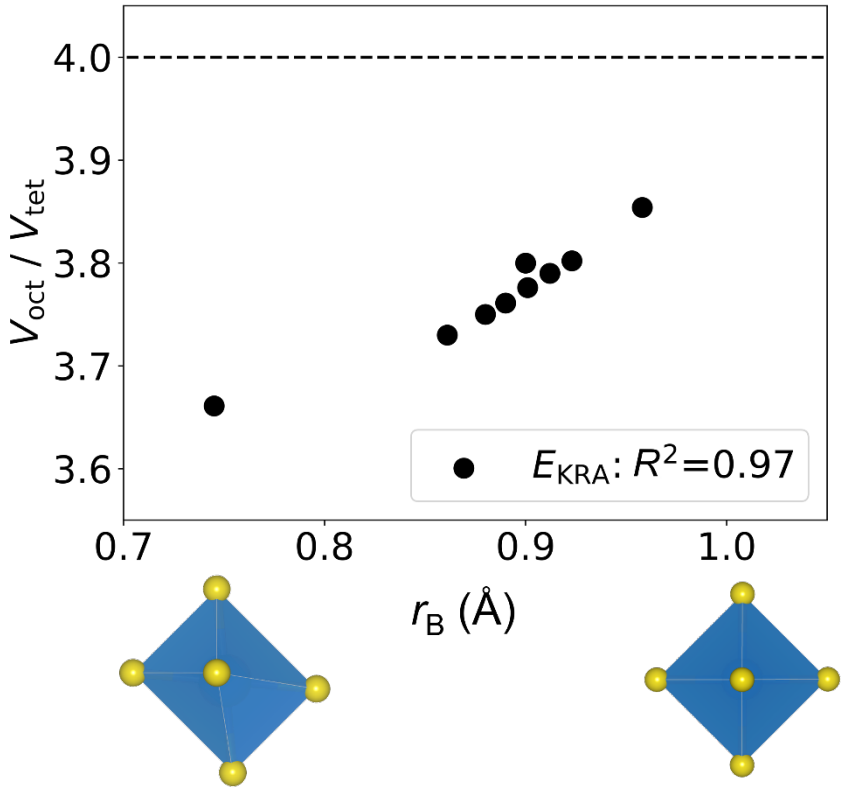

Figure S16. The dependence of the ratio of the volume of the octahedral site and the volume of the tetrahedral site on the ionic radius r_B of the metal B. In the regular (distortion free) system the volume of the octahedron is four times larger than the volume of the tetrahedron. As a consequence of trigonal distortion this ratio is decreasing with decreasing r_B.

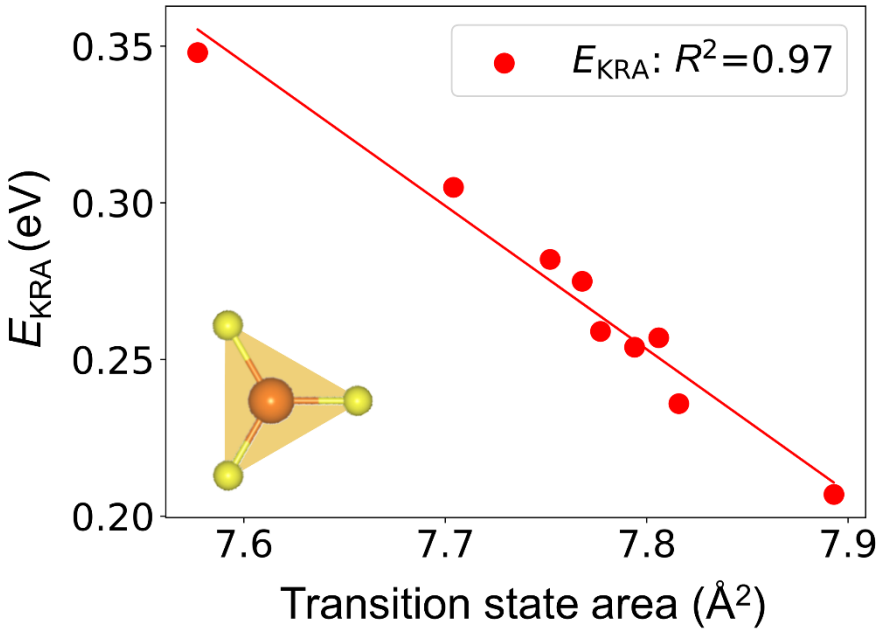

Figure S17. Kinetically resolved barrier E_{KRA} as function of the transition state area. Increasing the area leads to a stabilization of the transition state and decreases E_{KRA}.

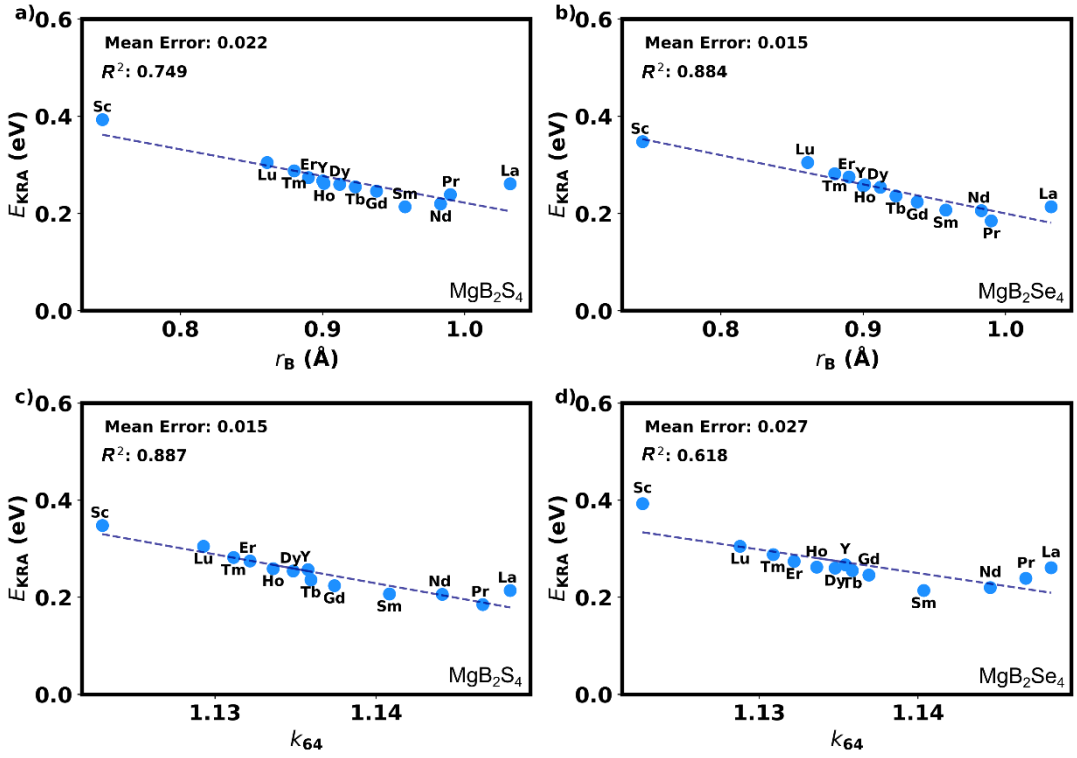

Figure S18. The linear regressions for E_{KRA} as function of the ionic radius r_B of the B metal are shown with dashed lines for a) the MgB_2S_4 sulfide spinels and b) the MgB_2Se_4 selenide spinels including the mean error and R^2 values. The linear regressions for E_{KRA} as function of the ratio of the distance k_{64} including the mean error and R^2 values are shown for c) the MgB_2S_4 sulfide spinels and d) the MgB_2Se_4 selenide spinels.

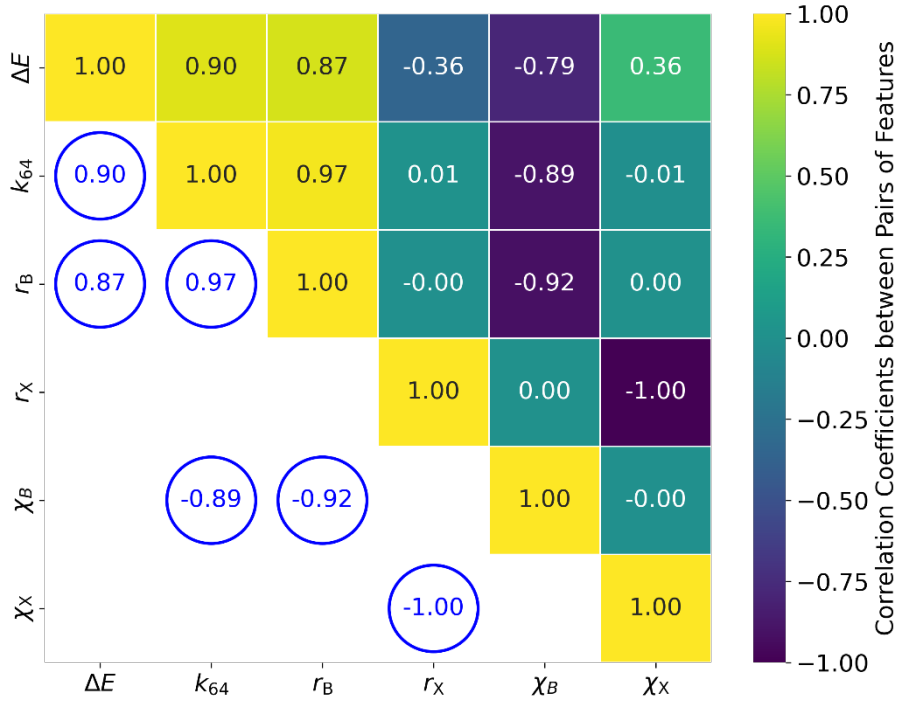

Figure S19. Pair-wise correlation heat map of preprocessed features: A heat map illustrating the correlation coefficients between pairs of features after preprocessing the dataset. Features include ΔE, k_{64}, r_B, r_X, χ_B, and χ_X. Highly correlated feature pairs are emphasized, with blue circles denoting the strength of correlation.

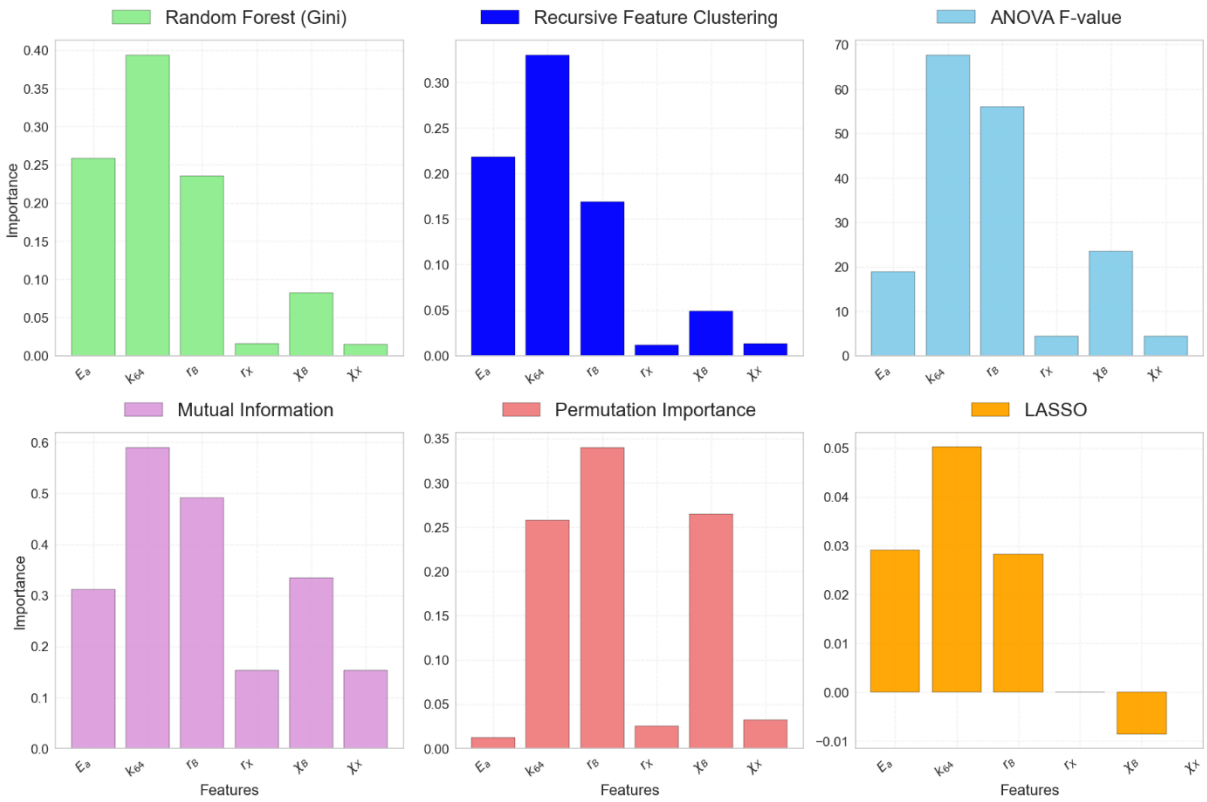

Figure S20. Feature importances for the class of chemical compounds (sulfides and selenides) under investigation, determined by the various techniques: a) Recursive Feature Clustering (RFC) b) Random Forest Gini, c) ANOVA F-value, d) Mutual Information, e) Permutation Importance and f) LASSO (Least Absolute Shrinkage and Selection Operator). The bar plot shows the magnitude and direction of LASSO coefficients or importance for influential features. Non-zero coefficients indicate significant contributions, with positive values suggesting a positive correlation and negative values indicating a negative correlation with ΔE. Color intensity reflects coefficient magnitude.

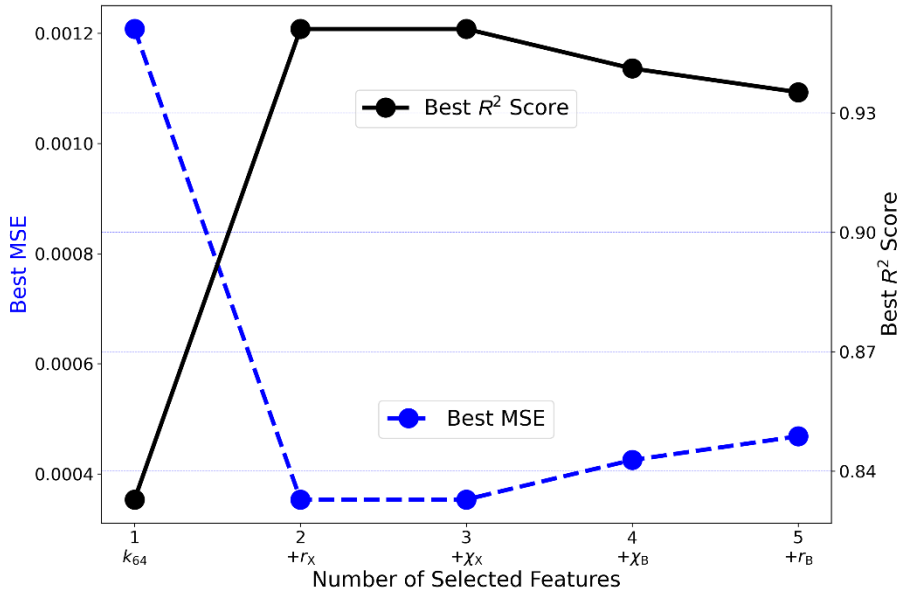

Figure S21. Optimized impact of selected chemical features on linear regression model performance (excluding E_a(th)) for prediction of ΔE: The plot illustrates the trade-off between the number of selected features (excluding E_a(th)) and model performance, showcasing the best mean square error (MSE) and *R*-squared (R^2) scores for each feature subset. The best feature combinations were determined through exhaustive search, showcasing the trade-off between model complexity and predictive accuracy. The results highlight the optimal feature combinations for achieving improved predictive accuracy in the absence of the activation energy E_a(th).

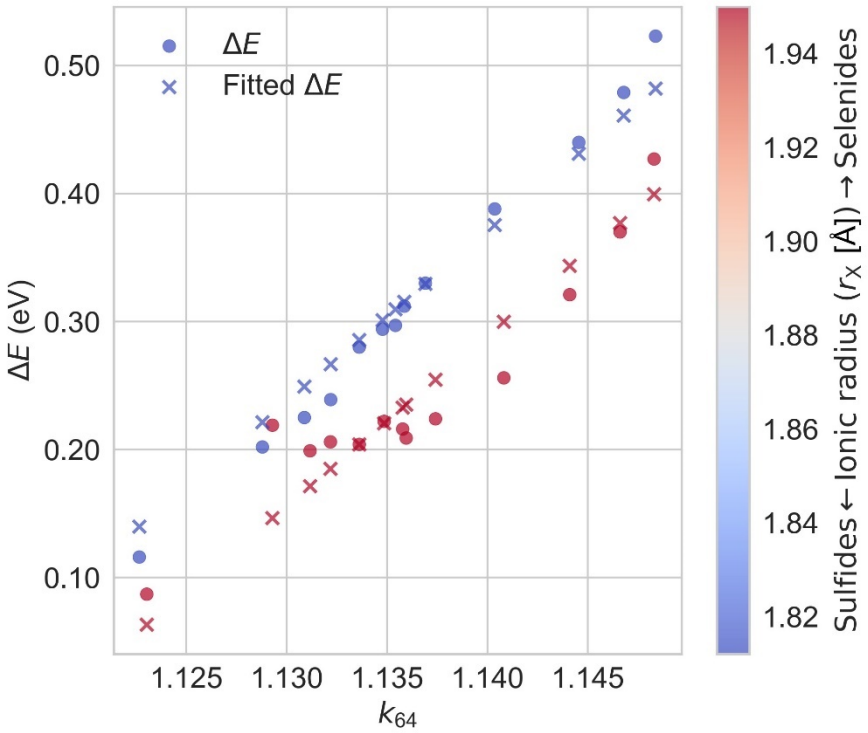

Figure S22. Comparison of actual and fitted ΔE values against r_X and k_{64}. The scatter plot depicts actual ΔE values, with red circles representing selenides and blue circles representing sulfides. Cross marks in corresponding colors represent the fitted data, illustrating the optimized linear regression model's proficiency in capturing the relationship between the target variable (ΔE) and the features r_X and k_{64}.

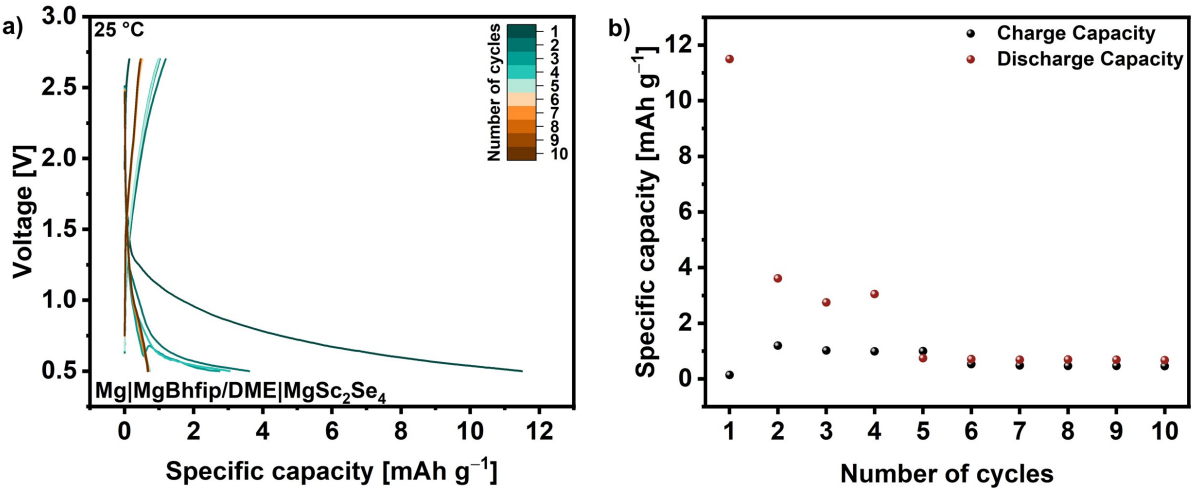

Figure S23. a) Galvanostatic discharge/charge voltage profiles of a cathode with $MgSc_2Se_4$ as active material recorded at room temperature over ten cycles between 0.5-2.7 V at a current rate of 10 mA g^{-1} and b) the very low specific capacities of discharge and charge steps represent the high redox stability of $MgSc_2Se_4$ in the examined voltage range.

Table S1. Crystallographic data for $MgSc_2Se_4$[1] (one-step synthesis) obtained from Rietveld refinement, based on the corresponding XRD pattern measured using Cu K_α radiation.

Crystallographic information	**Result**
Crystal system	Cubic
Space group	Fd-3m
Lattice parameters	a = b = c = 11.12781 Å
Cell volume	1377.936 Å^3
Density	4.146 g cm^{-3}
X^2	2.18
R_{wp}	11.0
R_{exp}	7.45
Bragg R-factor	5.00
RF-factor	3.74
GoF-index	1.5

Table S2. Crystallographic data for $MgTm_2Se_4$ (one-step synthesis) obtained from Rietveld refinement, based on the corresponding XRD pattern measured using Cu K_α radiation.

Crystallographic information	**Result**
Crystal system	Cubic
Space group	Fd-3m
Lattice parameters	a = b = c = 11.46260 Å
Cell volume	1506.085 Å^3
Density	5.224 g cm^{-3}
X^2	3.35
R_{wp}	19.6
R_{exp}	10.73
Bragg R-factor	13.6
RF-factor	12.2
GoF-index	1.8

Table S3. Crystallographic data for $MgEr_2Se_4$ (one-step synthesis) obtained from Rietveld refinement, based on the corresponding XRD pattern measured using Cu K_α radiation.

Crystallographic information	**Result**
Crystal system	Cubic
Space group	Fd-3m
Lattice parameters	a = b = c = 11.47062 Å
Cell volume	1509.248 Å^3
Density	5.106 g cm^{-3}
X^2	17.7
R_{wp}	26.5
R_{exp}	6.30
Bragg R-factor	13.7
RF-factor	14.9
GoF-index	4.2

Table S4. Crystallographic data for MgY_2Se_4 (one-step synthesis) obtained from Rietveld refinement, based on the corresponding XRD pattern measured using Cu K_α radiation.

Crystallographic information	**Result**
Crystal system	Cubic
Space group	Fd-3m
Lattice parameters	a = b = c = 11.57293 Å
Cell volume	1549.994 Å^3
Density	4.807 g cm^{-3}
X^2	7.48
R_{wp}	20.6
R_{exp}	7.53
Bragg R-factor	7.97
RF-factor	5.42
GoF-index	2.7

Table S5. Crystallographic data for $MgSc_2Se_4$[1] (two-step synthesis) obtained from Rietveld refinement, based on the corresponding XRD pattern measured using Cu K_α radiation.

Crystallographic information	Result
Crystal system	Cubic
Space group	Fd-3m
Lattice parameters	$a = b = c$ = 11.12973 Å
Cell volume	1378.650 Å^3
Density	4.144 g cm^{-3}
X^2	2.29
R_{wp}	8.56
R_{exp}	5.66
Bragg *R*-factor	3.43
RF-factor	2.17
GoF-index	1.5

Table S6. Crystallographic data for $MgTm_2Se_4$ (two-step synthesis) obtained from Rietveld refinement, based on the corresponding XRD pattern measured using Cu K_α radiation.

Crystallographic information	Result
Crystal system	Cubic
Space group	Fd-3m
Lattice parameters	$a = b = c$ = 11.47505 Å
Cell volume	1510.998 Å^3
Density	6.428 g cm^{-3}
X^2	12.4
R_{wp}	18.2
R_{exp}	5.17
Bragg *R*-factor	10.7
RF-factor	7.13
GoF-index	3.5

Table S7. Crystallographic data for $MgEr_2Se_4$ (two-step synthesis) obtained from Rietveld refinement, based on the corresponding XRD pattern measured using Cu K_α radiation.

Crystallographic information	**Result**
Crystal system	Cubic
Space group	Fd-3m
Lattice parameters	$a = b = c$ = 11.50949 Å
Cell volume	1524.643 Å^3
Density	4.790 g cm^{-3}
X^2	4.84
R_{wp}	24.7
R_{exp}	11.23
Bragg *R*-factor	13.0
RF-factor	9.75
GoF-index	2.2

Table S8. Crystallographic data for MgY_2Se_4 (two-step synthesis) obtained from Rietveld refinement, based on the corresponding XRD pattern measured using Cu K_α radiation.

Crystallographic information	**Result**
Crystal system	Cubic
Space group	Fd-3m
Lattice parameters	$a = b = c$ = 11.57079 Å
Cell volume	1549.134 Å^3
Density	4.375 g cm^{-3}
X^2	9.61
R_{wp}	16.8
R_{exp}	5.41
Bragg *R*-factor	6.74
RF-factor	3.91
GoF-index	3.1

Table S9. Mass *m* and thickness *d* of the UiO66-MgIL layer in the SS|UiO66-MgIL|SS cells.

Name of cell	UiO66-MgIL	*m*(UiO66-MgIL) [mg]	*d*(UiO66-MgIL) [mm]
MOF1[1]	UiO66-MgIL-1	80	0.60
MOF2	UiO66-MgIL-2	80	0.59

Table S10. Mass *m* and thickness *d* of MgB_2Se_4 pellets and UiO66-MgIL layers (sum of both layers) in the SS|UiO66-MgIL|MgB_2Se_4|UiO66-MgIL|SS cells.

Name of cell	spinel	*m*(MgB_2Se_4) [mg]	*d*(MgB_2Se_4) [mm]	UiO66-MgIL	*m*(UiO66-MgIL) [mg]	*d*(UiO66-MgIL) [mm]
Sc160[1]	$MgSc_2Se_4$	160	0.80	UiO66-MgIL-1	80	0.56
Sc190[1]	$MgSc_2Se_4$	190	0.88	UiO66-MgIL-1	80	0.56
Sc220[1]	$MgSc_2Se_4$	220	1.10	UiO66-MgIL-1	80	0.38
Sc250[1]	$MgSc_2Se_4$	250	1.14	UiO66-MgIL-1	80	0.56
Sc280[1]	$MgSc_2Se_4$	280	1.40	UiO66-MgIL-1	80	0.59
Tm160	$MgTm_2Se_4$	160	0.46	UiO66-MgIL-2	80	0.61
Tm220	$MgTm_2Se_4$	220	0.62	UiO66-MgIL-2	80	0.65
Tm280	$MgTm_2Se_4$	280	1.00	UiO66-MgIL-2	80	0.54
Er160	$MgEr_2Se_4$	160	0.50	UiO66-MgIL-2	80	0.60
Er220	$MgEr_2Se_4$	220	0.68	UiO66-MgIL-2	80	0.58
Er280	$MgEr_2Se_4$	280	0.82	UiO66-MgIL-2	80	0.58
Y160	MgY_2Se_4	160	0.72	UiO66-MgIL-2	80	0.58
Y220	MgY_2Se_4	220	0.86	UiO66-MgIL-2	80	0.55
Y280	MgY_2Se_4	280	1.26	UiO66-MgIL-2	80	0.56

Table S11. Overview of resistances *R* obtained from data fitting ([a]) or due to direct calculation from data points ([b]), exemplarily shown for the room temperature (25 °C) impedance measurements of all SS|UiO66-MgIL|SS and SS|UiO66-MgIL|MgB_2Se_4|UiO66-MgIL|SS cells. While for the fitting of the SS|UiO66-MgIL|SS cells MOF-1 and MOF-2 the equivalent circuit in **Figure 3b** was applied, the remaining spinel-containing cells were fitted with the equivalent circuit in **Figure 3c**. In addition, for these cells, $R1_{ion}$ and R_{ion}(UiO66-MgIL) were calculated by **Equation S1** ([c]). Note: The electronic resistance $R2_{el}$ is not listed since it is impossible to determine reliable results by the applied equivalent circuit, as described in our earlier work.[1]

Name of cell	$R1_{ion}$ [Ω]	R_{ion}(UiO66-MgIL) [Ω]	$R2_{ion}$ [Ω]	$R_{ion}(MgB_2Se_4)$ [Ω]	$R1_{ion}+R2_{ion}$ [Ω]	R_{ion}(SEs) [Ω]
MOF1[1]	806[a]	806[b]	-	-	806[a]	806[b]
MOF2	273[a]	274[b]	-	-	273[a]	274[b]
Sc160[1]	752[c]	752[c]	1870[a]	1862[b]	2622[a]	2614[b]
Sc190[1]	752[c]	752[c]	2532[a]	2536[b]	3284[a]	3287[b]
Sc220[1]	510[c]	510[c]	2974[a]	2875[b]	3484[a]	3386[b]
Sc250[1]	752[c]	752[c]	5169[a]	5161[b]	5921[a]	5912[b]
Sc280[1]	792[c]	792[c]	7564[a]	7466[b]	8356[a]	8258[b]
Tm160	283[c]	283[c]	631[a]	592[b]	914[a]	875[b]
Tm220	301[c]	302[c]	1289[a]	1180[b]	1590[a]	1482[b]
Tm280	250[c]	251[c]	3199[a]	3136[b]	3449[a]	3386[b]
Er160	278[c]	279[c]	1282[a]	1003[b]	1560[a]	1282[b]
Er220	269[c]	269[c]	2323[a]	2074[b]	2592[a]	2343[b]
Er280	269[c]	269[c]	2881[a]	2646[b]	3150[a]	2915[b]
Y160	269[c]	269[c]	3534[a]	3530[b]	3803[a]	3799[b]
Y220	254[c]	255[c]	5491[a]	5490[b]	5745[a]	5745[b]
Y280	259[c]	260[c]	11743[a]	11748[b]	12002[a]	12008[b]

Since the total UiO66-MgIL layer thickness in the SS|UiO66-MgIL|MgB_2Se_4|UiO66-MgIL|SS cells (see Table S10) can vary to those used in the SS|UiO66-MgIL|SS reference cells (see Table S9), the impedances of the UiO66-MgIL were adapted to the layer thickness used by Equation S1:

$$R_{ion}(i) = \frac{d(\text{UiO66-MgIL})}{d(\text{UiO66-MgIL-Ref.})} R_{ion}(i\text{-Ref.}) \quad \text{(S1)}$$

i = UiO66-MgIL, $R1_{ion}$

Ref. = MOF1 or MOF2

For the $MgSc_2Se_4$-based cells the reference cell MOF1 was used, while MOF2 was the reference cell for the $MgTm_2Se_4$-, $MgEr_2Se_4$- and MgY_2Se_4-based cells.

Table S12. Comparison of computational migration barriers for spinel compounds $MgSc_2Se_4$, $MgEr_2Se_4$, MgY_2Se_4 and $MgTm_2Se_4$ determined using different exchange-correlation functionals (PBE: Perdew-Burke-Ernzerhof[2]; SCAN: Strongly Constrained and Appropriately Normed[3]) and settings with experimental migration barriers. The supercell volume was either kept fixed (fix) or relaxed (rel) to allow for possible distortion due to the introduction of a vacancy in the system. Moreover, the influence of formal charge compensation due to a uniform background charge (chg) was tested. Overall, the influence of volume relaxation and formal charge compensation were found to be rather limited while SCAN calculations were found to be in better agreement with the experimentally determined migration barriers.

compound	PBE (fix) [meV]	PBE (rel) [meV]	PBE (fix, chg) [meV]	SCAN (fix, chg) [meV]	SCAN (fix) [meV]	experiment [meV]
$MgSc_2Se_4$	336	339	343	367	392	386
$MgTm_2Se_4$	334	362	331	368	381	381
$MgEr_2Se_4$	333	357	330	365	378	382
MgY_2Se_4	348	349	341	361	365	408

References

[1] C. Glaser, Z. Wei, S. Indris, P. Klement, S. Chatterjee, H. Ehrenberg, Z. Zhao‐Karger, M. Rohnke, J. Janek, *Adv. Energy Mater.* **2023**, *13*, 2301980.

[2] J. P. Perdew, K. Burke, M. Ernzerhof, *Phys. Rev. Lett.* **1996**, *77*, 3865.

[3] J. Sun, A. Ruzsinszky, J. P. Perdew, *Phys. Rev. Lett.* **2015**, *115*, 36402.